Editors' Suggestion | Featured in Physics

Experimental Realization of a Fermionic Spin-Momentum Lattice

Paul Lauria,[1] Wei-Ting Kuo,[1] Nigel R. Cooper,[2] and Julio T. Barreiro[1]
[1]Department of Physics and Astronomy, University of California San Diego, La Jolla, California 92093, USA
[2]T.C.M. Group, Cavendish Laboratory, University of Cambridge, Cambridge CB3 0HE, United Kingdom

(Received 18 March 2022; accepted 10 May 2022; published 15 June 2022)

We experimentally realize a spin-momentum lattice with a homogeneously trapped Fermi gas. The lattice is created via cyclically rotated atom-laser couplings between three bare atomic spin states, and are such that they form a triangular lattice in a synthetic spin-momentum space. We demonstrate the lattice and explore its dynamics with spin- and momentum-resolved absorption imaging. This platform will provide new opportunities for synthetic spin systems and the engineering of topological bands. In particular, the use of three spin states in two spatial dimensions would allow the simulation of synthetic magnetic fields of high spatial uniformity, which would lead to ultranarrow Chern bands that support robust fractional quantum Hall states.

DOI: 10.1103/PhysRevLett.128.245301

Ultracold atoms in optical lattices have been established as an important tool for the quantum emulation of condensed matter models [1], especially those with topological features [2,3]. The inherent tunability afforded by optical lattices provides access to a variety of parameter regimes, which has proved essential in the seminal realizations of topological phases in ultracold matter [4–7]. Since then, efforts to study topology in other systems have led to the exploration of synthetic dimensions [8,9], which provide internal degrees of freedom beyond those afforded by the trapping geometry and have enabled a new generation of experiments [10].

Several approaches to synthetic dimensions have been experimentally realized. Real-space lattices augmented with spin-orbit coupling (SOC) connect spin "lattice" sites via momentum exchange, creating Hall cylinders pierced by magnetic flux in a synthetic position-spin space [11–18], or creating Hall ribbons in optical clock experiments [19–22]. Real-space lattices are not always needed; SOC itself can provide synthetic degrees of freedom, which can act as a potent generator of Berry curvature [23–28] or provide control parameters for Hamiltonian engineering [29,30]. Synthetic lattices entirely in momentum space [31,32] have been realized, and, with carefully engineered hopping schemes, have proven topological [33–36]. Recently, a synthetic lattice of Rydberg states has been employed for the study of a Su-Schrieffer-Heeger model [37], and a synthetic dimension of trap states created with patterned light [38].

Lattices composed of spin and momentum states, or spin-momentum (SM) lattices, have been proposed [39] as a platform to exhibit topological features, with some schemes potentially realizing the Laughlin state of the fractional quantum Hall effect [40,41]. As a step toward this, we realize a fermionic spin-momentum lattice using SOC and three atomic Zeeman spin states. Previous experiments using spin-momentum lattices utilized bosons in a single dimension [42,43], and used a real-space lattice with lattice-band pseudospins [44]. Recently, a two-spin bosonic SM lattice has been implemented in an optical cavity [45]. Here, by providing sufficient links between three spin sites, we build a lattice of fermions in a 2D spin-momentum space, without a traditional scalar optical lattice. This platform increases the flexibility of the synthetic dimension approach. In particular, the use of three spin states in two spatial dimensions allows the simulation of synthetic magnetic fields of high spatial uniformity, which lead to ultranarrow Chern bands that support robust fractional quantum Hall states [41,46].

Implementation.—The synthetic lattice is composed of three Zeeman spin states in the $^1S_0(F = 9/2)$ ground state of ^{87}Sr, labeled $X \equiv |m_F = -9/2\rangle$, $Y \equiv |m_F = -7/2\rangle$, $Z \equiv |m_F = -5/2\rangle$. In a momentum-dependent manner, the spins are cyclically coupled by up to nine Raman lasers intersecting at 120°. In the rotating-wave approximation, we describe the atom-laser coupling as

$$\hat{V} = \Omega_{mn} e^{i(\mathbf{k}_R \cdot \mathbf{r} + \varphi_i - \varphi_j)} |m\rangle\langle n| + \text{H.c.}, \tag{1}$$

where $m \neq n$ runs over the states X, Y, Z, $|\mathbf{k}_R| = |\mathbf{k}_i - \mathbf{k}_j| = k_L \sin^2(\theta/2)$ is the magnitude of the single-photon recoil wave vector with $i \neq j$ denoting the beams driving a particular m-n coupling, Ω_{mn} is the coupling strength, and $\theta = 120°$ is the angle between any pair of beams. The single-photon recoil energy is $E_R = (\hbar k_R)^2/2m = \hbar \times 22.7$ kHz. The phase differences $\varphi_i - \varphi_j$ are set to zero in the experiment, but we note that setting nonzero phases is at the heart of the ultranarrow-band optical flux lattice experiment [41].

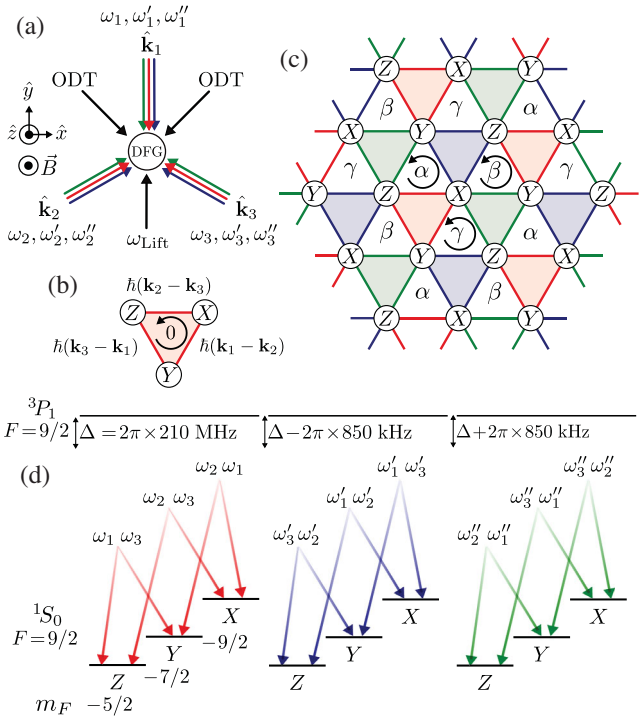

FIG. 1. Experiment schematic and coupling details. (a) A degenerate Fermi gas (DFG) in a crossed optical dipole trap (ODT) is exposed to cyclic Raman couplings between three internal spin states; see text for details. A beam ω_{Lift} provides a nonlinear energy splitting between the states. (b) States X, Y, Z are connected among themselves through spin-momentum exchange in units of $\hbar\delta\mathbf{k}_{ij} = \hbar(\mathbf{k}_i - \mathbf{k}_j)$. With a single set of beams, no net phase pickup is possible, denoted by the 0. (c) The couplings form a lattice in momentum space. Atoms encircling plaquettes labeled by α, β, γ can pick up a net phase. The link color indicates the frequency set in (d) to which the beams belong. (d) Details of the resonant couplings between the three internal states labeled X, Y, and Z, which represent the nuclear angular momentum projections $m_F = -9/2, -7/2, -5/2$, respectively, in the $^1S_0(F = 9/2)$ ground state. We circularly exchange the roles of the frequencies colored red (ω_i) in the blue (ω_i') and green (ω_i'') coupling sets.

The setup implementing the optical couplings in Eq. (1) is shown in Fig. 1(a). Up to three running-wave triplets of beams are incident on a degenerate Fermi gas (DFG) spin polarized mostly into state $|X\rangle$ with $T/T_F = 0.36(5)$, where T_F is the Fermi temperature. Each beam $\hat{\mathbf{k}}_i$ contains up to three frequencies ω_i, ω_i', ω_i'', such that the energy difference between any two frequencies $\omega_i['('')] - \omega_j['('')]$ matches an energy difference in the X, Y, Z manifold. These beams provide a Raman coupling between states, as in Fig. 1(b). The quantization axis is defined by a $\hat{z}$-oriented magnetic field $B \approx 9.3$ G, along which we align the linear polarization of a beam ω_{Lift} [15,47,48] providing a strong ac Stark shift that lifts the degeneracy of the states X, Y, Z. The coupling beam polarizations are linear and angled at $33(1)°$ with respect to the xy plane, projecting approximately equal intensity among the possible Raman transition types π, $\sigma^{\pm}$. When using all nine frequencies, the beams form an infinite lattice in spin-momentum space, as in Fig. 1(c). Since the average starting atomic momentum $\langle p \rangle \ll 4\hbar k_R$, the fermions initially occupy only a small spread of states $|X/Y/Z, \mathbf{q} \approx 0\rangle$, where $\mathbf{q}$ is the quasimomentum. After engaging the coupling beams, atoms with differing spin or $\mathbf{q}$ occupy adjacent spin-momentum lattices, shifted by their corresponding quantum numbers. These lattices are not tight binding, in the sense that *in situ* motion is constrained only by the overall harmonic trap, allowing particles of different spin and $\mathbf{q}$ to mix. Unlike a square lattice—which does not readily allow for nonzero Chern number—this triangular lattice naturally breaks inversion symmetry and allows for magnetic flux. We note that nonzero gauge flux is possible only on the upward-pointing triangles, corresponding to momentum transfers involving all three frequency sets.

As shown in Fig. 1(d), the coupling beams utilize the dipole-forbidden transition $^1S_0(F=9/2) \to {}^3P_1(F=9/2)$, detuned below resonance by $\Delta/2\pi = 210$ MHz. The transition's narrow linewidth $\Gamma/2\pi = 7.4$ kHz allows coherent manipulation with minimal spontaneous emission, and no significant destructive interference [49,50] arises from the terahertz-separated fine structure states $^3P_0$ and $^3P_2$. In order to make each triplet unique, the upper-state detunings of the blue and green couplings are shifted by $\mp 37E_R/\hbar$, larger than the $\approx 7.5E_R/\hbar$ energy splittings. The role of the frequency ω_i in beam $\mathbf{k}_i$ is circularly rotated among the three triplets, such that all frequencies resonantly couple all spin states.

In order to realize the lattice, careful attention must be paid to the energy levels of X, Y, and Z, which are naturally degenerate. Since the ground states have $J = 0$—rendering Zeeman shifts insignificant at our bias field—we use an ac Stark shift approach. Further leveraging the narrow-line intercombination transition, the lift beam ω_{Lift} is operated at 434.830 043(5) THz, midway between the hyperfine resonance lines $^1S_0(F = 9/2) \to {}^3P_1(F = 7/2)$ and $^1S_0(F = 9/2) \to {}^3P_1(F = 9/2)$. This light was designed to produce a strong tensor shift $\epsilon = 1.76E_R/\hbar$ of the X state, allowing each pair of Raman beams to uniquely couple two spin-momentum states. A necessary condition of the spin-momentum lattice model is that the coupling strengths $\Omega \ll \epsilon$. The coupling strengths here are $\Omega \approx 0.5E_R/\hbar$ [51].

Experimental sequence.—In our newly built apparatus, we source ^{87}Sr from a commercial atomic oven from AOSense, which includes an integrated Zeeman slower and 2D magneto-optical trap (MOT) optics. After two MOT loading and cooling stages lasting 7 s [63,64], the atoms are loaded into a crossed 1064 nm optical dipole trap (ODT) with an initial temperature of ≈ 2 μK. The vertical [horizontal] trapping frequency is ramped up to 2.160(5) kHz [313(1), 397(2) Hz], at which point we spin polarize

the sample with a series of pulses resonant with the different m_F states via the $^1S_0(F=9/2) \rightarrow {}^3P_1(F=9/2)$ transition [51,65,66]. The ODT frequencies are then lowered back to ≈1 kHz vertically, and forced evaporation proceeds over the next 10 s, finally reaching a quantum-degenerate sample. Without spin polarization, we routinely achieve $T/T_F = 0.20$, where T_F is the Fermi temperature, rising to $T/T_F = 0.36(5)$ when spin polarized. Evaporation ends at mean geometric trap frequency $\bar{\omega} = (\omega_x\omega_y\omega_z)^{1/3} = 71.4(1)$ Hz, yielding a 50 nK Fermi gas. Immediately following evaporation, the sample is spin polarized in the state $X(80 \pm 7\%)$, and the ac Stark shifting beam ω_{Lift} is ramped on in 0.5 ms. Via optical Stern-Gerlach imaging [67], we verify that this timescale does not alter the spin polarization. We then introduce the coupling beams with a turn-on time of < 1 μs.

We demonstrate the spin-momentum lattice in Fig. 2. In order to fill more sites, we emulate motion along a single dimension by subjecting the atoms to an inertial force [17] along $\hat{\mathbf{k}}_1$, ramping all three of that beam's frequencies at a rate $\hbar\partial_t(\omega_1, \omega_1', \omega_1'') = 16.607E_R/\mathrm{ms}$ [68]. Hopping to neighboring sites is made favorable when the frequency difference between two coupling beams matches the energy and recoil shifts between states, providing enhanced state transfer between initial state $|X, \mathbf{q}\rangle$ and $|X, \mathbf{q} - \mathbf{K}\rangle$, $|Y, \mathbf{q} - \mathbf{K}\rangle$, $|Z, \mathbf{q} - \mathbf{K}\rangle$ for some reciprocal lattice vectors $\mathbf{K} = n_1\mathbf{q}_1 + n_2\mathbf{q}_2$ with integers n_1, n_2. After a varying sweep time, all optical fields are quenched off, releasing the atoms from the harmonic trap. Atoms that have tunneled to different lattice sites acquire a concomitant increase in momentum, in discrete units of the two-photon Raman momentum $\hbar k_R = \sqrt{3}/2\hbar k_L$. The lattice sites become spatially resolved after 12 ms time of flight, since the starting momentum distribution's full width at half maximum is $1.05(1)\hbar k_L$ and external heating by spontaneous emission from $^3P_1$ is minimal [51]. The atoms are then absorption imaged in the xy plane using the $^1S_0 \rightarrow {}^1P_1$ transition at 461 nm ($\Gamma_{461}/2\pi = 30$ MHz), which images all spins with approximately equal efficiency [69]. The bias magnetic field is kept on at all times, in order to maintain the spin quantization axis.

The individual columns of Fig. 2 demonstrate spin- and momentum-resolved imaging at various quench times. Sweep time is indicated by the final frequency deviation of the swept beam, in units of E_R. Intuitively, one would not expect stationary atoms ($\langle p \rangle \approx 0$) to tunnel before at least overcoming the recoil shift $4E_R$, and we observe this in the experiment. Denoting transferred momentum by $\hbar\delta k_{ij} = \hbar(|\mathbf{k}_i - \mathbf{k}_j|)$, and referring to beam triplets by their colors in Fig. 1(d), when the sweep reaches $4E_R$ we see beams ω_1, ω_2 from the red triplet driving the corresponding Raman transition $|X, 0\rangle \rightarrow |Y, \hbar\delta k_{12}\rangle$; similarly, the green beams ω_1', ω_3' allow $|X, 0\rangle \rightarrow |Z, \hbar\delta k_{13}\rangle$. By $8E_R$, atoms have firmly populated sites $|Y, \hbar\delta k_{12}\rangle$, $|Z, \hbar\delta k_{13}\rangle$, with initially-faster-moving atoms beginning to populate

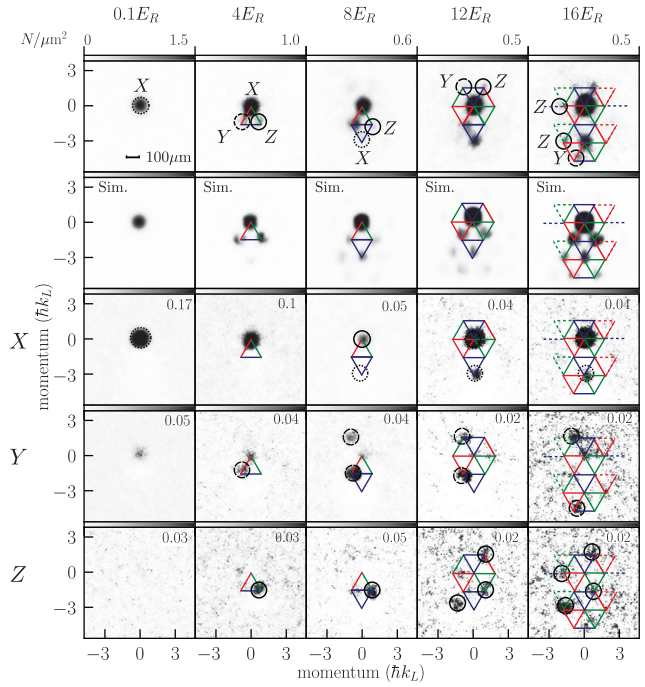

FIG. 2. Demonstration of the spin-momentum lattice. A DFG is exposed to the nine-beam coupling scheme, with the $\mathbf{k}_1$ triplet frequency swept in order to populate more lattice sites; see text for details. The sweep progress is indicated in units of recoil energy E_R. The top row shows spin-unresolved momentum-space images, in which the lattice is most clearly evident. The second row shows the predicted dynamics from simulations (Sim.). Subsequent rows show spin-resolved images. In each row, we draw a link connecting each lattice site with a color corresponding to the involved beams, as detailed in Fig. 1(d). In the top row, we encircle and label each new lattice site as it becomes apparent during the sweep, and in the spin-resolved rows the expected populations are also encircled. As a guide to the eye, the links are also drawn across all rows. Each image is an average of ≈100 experimental runs taken at 12 ms time of flight. The peak atomic density is indicated in the top right of each image, in units of N atoms per μm^2.

the site $|X, p = -3\hbar k_L\rangle$, completing a traversal of the first Brillouin zone. By $12E_R$, more atoms have tunneled through the Brillouin zone, and the momentum center of mass proceeds downward at $16E_R$; imaging becomes increasingly difficult due to the lower atom density, so we terminate here. As a consistency check, we also demonstrate spin-resolved imaging using spin blasts [51,70] in order to verify that sites on the SM lattice are of the expected spin projection m_F. We observe good consistency with the SM lattice model as drawn in Fig. 1(d), although mechanical effects of the spin blasts can mask some lattice sites, notably, the X site at $\mathbf{p} = -3\hbar k_L\hat{y}$ (see the Appendix). Our model shows qualitative agreement with the data for a scaled value of the measured Rabi coupling strengths. Some disagreement is evident, especially at the lattice sites with momenta $\mathbf{p} = \sqrt{3}/2\hbar k_L$,

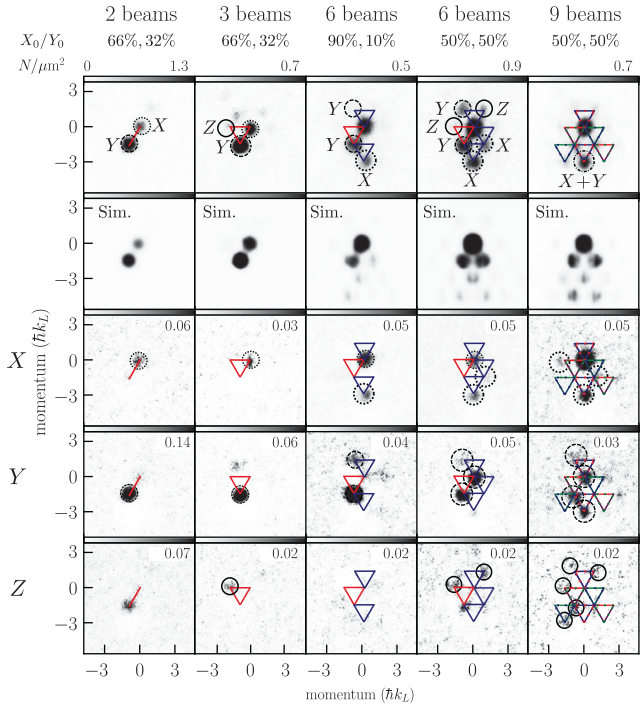

FIG. 3. Building the spin-momentum lattice; all images taken at a common sweep time of $12E_R$. The drawn links and circles are as described in Fig. 2, with the second row showing the predicted dynamics (Sim.). Each removed frequency corresponds to a missing link in the full lattice setup, allowing the exploration of quasi-1D SOC in the first column, to 2D SOC in the second column, culminating in the full lattice shown in the last column. The multiply-colored links in the last two columns indicate two SM lattices simultaneously overlaid: a two-state configuration, in which the experiment began with equal populations of X, Y.

which are predicted to have a stronger amplitude than is observed. We attribute these mismatches to off-resonant effects not included in our effective Hamiltonian [51].

The lattice scheme presented here is readily tunable. Although the full spin-momentum lattice is composed of nine frequencies, we can remove links between lattice sites at will. We explore this flexibility in Fig. 3, where we show the driven dynamics experiment of Fig. 2, but now with all images taken at a common sweep time $12E_R$. In the two-beam scheme, composed of a single frequency in each of two beams $\hat{k}_1, \hat{k}_2$, we have reduced the system to a 1D SOC model between an effective spin-up $|\uparrow\rangle = |X, \mathbf{q}\rangle$ and spin-down $|\downarrow\rangle = |Y, \mathbf{q}\rangle$ [70,71]. In the three-beam case, with a single frequency in each of the $\hat{k}_1$, $\hat{k}_2$, and $\hat{k}_3$ beams, we have a 2D spin-orbit coupling [25,72,73] cyclically linking the three states X, Y, Z. The six-beam case consists of beams $\hat{k}_1$, $\hat{k}_2$, and $\hat{k}_3$ each possessing two frequencies, labeled by their colors red and blue as labeled in Fig. 1. In the last two columns, we explore the dynamics starting from an even spin mix of states X and Y, which, in the nine-beam experiment, can be visualized as two SM lattices overlapped on $\mathbf{p} = 0$.

Conclusion and outlook.—We have demonstrated a two-dimensional fermionic spin-momentum lattice without the use of standing waves. This adds to the wealth of cold atom synthetic dimension platforms available to study topological materials. The system's 15 ms lifetime exceeds our current experimental duration by a factor of 10, and could be further improved with increased Raman detuning Δ. The current lift beam strength imposes a 30 ms limit, which can be relaxed under appropriate conditions [51]. The number of visible lattice sites can be increased with larger Rabi coupling strengths, or by slowing the sweep rate, which would couple more atoms out of the $p \approx 0$ momentum class. The spin-resolved imaging presented here could be improved by using stronger blast pulses to overcome the Doppler shifts among the lattice's numerous momentum states.

This Letter launches a novel platform for exploring topological physics with optical flux lattices. The natural extension of this Letter would be to load the atoms adiabatically into the lowest band and set nonzero coupling phases such that a gauge flux appears on the plaquettes labeled α, β, γ in Fig. 1. The topology of the band structure could then be probed using established anomalous velocity techniques [6,17,74], which involve accelerating the dressed atoms in the same manner as done here. Demonstrating this topology would enable the exploration of many-body fractional Hall states [41]. In the present experiment, spin-contact interactions are not expected to play a significant role, but these interactions may be increased through the use of a vertical real-space lattice, as detailed further in Ref. [41] for ^{87}Rb, which we note has the same scattering length $\approx 100a_0$ as ^{87}Sr.

All data associated with this publication can be found at [75].

We would like to thank C. Yu for assistance in constructing an early version of the experiment. We thank S. Mossman for helpful discussions of the experimental design, and are grateful for helpful comments from I. Spielman. We acknowledge support from the National Science Foundation Award No. 1752630, EPSRC Grant No. EP/P009565/1 and a Simons Investigator Award.

Appendix: Spin-resolved imaging.—Atoms released from the SM lattice naturally spatially resolve according to their spin and momentum; however, in cases where the starting state is not pure or for verification purposes, it is necessary to have a means to resolve the spins. Directly imaging the spins using narrow-line absorption imaging [67] is impractical due to the low scattering cross section and relatively low atom density of Fermi gases. Furthermore, since the atoms are moving after they are released from the SM lattice, the use of optical Stern-Gerlach separation is not desirable because it will (necessarily) disturb the momentum distribution.

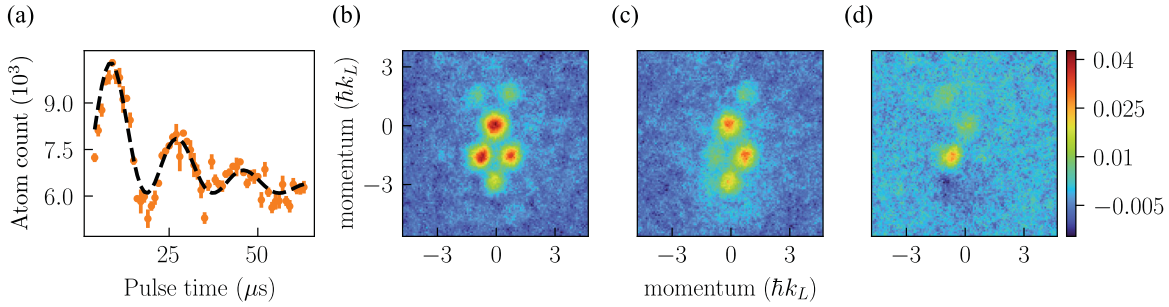

FIG. 4. Spin-resolved imaging process. (a) Spin-blast Rabi frequency calibrated by electron shelving of the $m_F = -7/2$ (Y) state. The fitted single-photon Rabi frequency is $\Omega = 335(1)$ kHz. (b) Averaged atom shot of the SM lattice at sweep time $8E_R$. (c) Spin-blast beam resonant with $m_F = -7/2$ applied to the SM lattice. (d) Subtraction of images (b) and (c), removing the common-mode background and revealing the locations of $m_F = -7/2$ atoms. A region of negative optical density forms at the locations of the blast-scattered atoms.

We instead visualize the spin dynamics with blast pulses [70], propagating in the xy plane, resonant with the narrow ${}^1S_0(F=9/2,m_F) \rightarrow {}^3P_1(F=9/2,m_F)$ transition at 689 nm. To be effective, the blast beam strength needs to be similar to the worst-case atomic Doppler shifts in the SM lattice $\Omega_{\text{Doppler}} \approx n \times 2\pi \times 4E_R = n \times 91$ kHz, where n is the number of photons absorbed in the SM lattice. Simultaneously, to avoid exciting neighboring m_F states, the blast strength must be smaller than the typical Zeeman splitting of the upper ${}^3P_1(F=9/2)$ states, here $2\pi \times 790$ kHz.

The beams are calibrated as in Fig. 4(a) with electron shelving [76]: atoms are excited into ${}^3P_1$ with a resonant 689 nm pulse for a time t, after which we apply a 4 μs pulse of 461 nm MOT light to blow away all remaining ground-state atoms. Atoms so "shelved" in the ${}^3P_1$ state do not interact with the 461 nm light; instead, the fraction projected onto the ground state is measured with absorption imaging after a brief 2 ms time of flight. The overall decay curve matches the ${}^3P_1$ natural lifetime of 22 μs. The SM lattice in Fig. 4(b) is subjected to this beam in Fig. 4(c), yielding the spin-resolved picture in Fig. 4(d) after subtracting the two images. Since the blast process relies on spontaneous emission, an atom can scatter (at most) a few photons before decaying to an adjacent m_F state, which is then transparent to the narrow-linewidth blast beam. This means the momentum acquired by the targeted atoms is comparable to the momentum of the atoms in the SM lattice, so some overlap is inevitable—as the negative optical density region in Fig. 4(d) shows. This effect can be particularly noticeable if the scattered atoms have strong geometric overlap with a region of interest, as seen in the X row of Fig. 2, particularly the $8E_R$ panel, which entirely masks the cloud at $\mathbf{p} = -3\hbar k_L \hat{y}$.

Furthermore, although the beam strengths are chosen to be comparable to the Doppler shifts, the efficiency of these single-tone blast pulses still decreases with increasing SM lattice photon absorption. To overcome this, a larger bias magnetic field would enable the use of stronger blast pulses. To overcome the geometric overlap issue, tilting the blast pulses out of plane would push targeted atoms out of the imaging focus region, more effectively removing them from the images.

[1] F. Schäfer, T. Fukuhara, S. Sugawa, Y. Takasu, and Y. Takahashi, Tools for quantum simulation with ultracold atoms in optical lattices, Nat. Rev. Phys. **2**, 411 (2020).

[2] N. Goldman, J. C. Budich, and P. Zoller, Topological quantum matter with ultracold gases in optical lattices, Nat. Phys. **12**, 639 (2016).

[3] N. R. Cooper, J. Dalibard, and I. B. Spielman, Topological bands for ultracold atoms, Rev. Mod. Phys. **91**, 015005 (2019).

[4] H. Miyake, G. A. Siviloglou, C. J. Kennedy, W. C. Burton, and W. Ketterle, Realizing the Harper Hamiltonian with Laser-Assisted Tunneling in Optical Lattices, Phys. Rev. Lett. **111**, 185302 (2013).

[5] M. Aidelsburger, M. Atala, M. Lohse, J. T. Barreiro, B. Paredes, and I. Bloch, Realization of the Hofstadter Hamiltonian with Ultracold Atoms in Optical Lattices, Phys. Rev. Lett. **111**, 185301 (2013).

[6] M. Aidelsburger, M. Lohse, C. Schweizer, M. Atala, J. T. Barreiro, S. Nascimbène, N. R. Cooper, I. Bloch, and N. Goldman, Measuring the Chern number of Hofstadter bands with ultracold bosonic atoms, Nat. Phys. **11**, 162 (2015).

[7] G. Jotzu, M. Messer, R. Desbuquois, M. Lebrat, T. Uehlinger, D. Greif, and T. Esslinger, Experimental realization of the topological Haldane model with ultracold fermions, Nature (London) **515**, 237 (2014).

[8] O. Boada, A. Celi, J. I. Latorre, and M. Lewenstein, Quantum Simulation of an Extra Dimension, Phys. Rev. Lett. **108**, 133001 (2012).

[9] A. Celi, P. Massignan, J. Ruseckas, N. Goldman, I. B. Spielman, G. Juzeliūnas, and M. Lewenstein, Synthetic Gauge Fields in Synthetic Dimensions, Phys. Rev. Lett. **112**, 043001 (2014).

[10] T. Ozawa and H. M. Price, Topological quantum matter in synthetic dimensions, Nat. Rev. Phys. **1**, 349 (2019).

[11] S.-L. Zhang and Q. Zhou, Shaping topological properties of the band structures in a shaken optical lattice, Phys. Rev. A **90**, 051601(R) (2014).
[12] M. Mancini, G. Pagano, G. Cappellini, L. Livi, M. Rider, J. Catani, C. Sias, P. Zoller, M. Inguscio, M. Dalmonte, and L. Fallani, Observation of chiral edge states with neutral fermions in synthetic Hall ribbons, Science **349**, 1510 (2015).
[13] B. K. Stuhl, H.-I. Lu, L. M. Aycock, D. Genkina, and I. B. Spielman, Visualizing edge states with an atomic Bose gas in the quantum Hall regime, Science **349**, 1514 (2015).
[14] J. H. Kang, J. H. Han, and Y. Shin, Realization of a Cross-Linked Chiral Ladder with Neutral Fermions in a 1D Optical Lattice by Orbital-Momentum Coupling, Phys. Rev. Lett. **121**, 150403 (2018).
[15] B. Song, L. Zhang, C. He, T. F. J. Poon, E. Hajiyev, S. Zhang, X.-J. Liu, and G.-B. Jo, Observation of symmetry-protected topological band with ultracold fermions, Sci. Adv. **4**, eaao4748 (2018).
[16] D. Genkina, L. M. Aycock, H.-I. Lu, M. Lu, A. M. Pineiro, and I. B. Spielman, Imaging topology of Hofstadter ribbons, New J. Phys. **21**, 053021 (2019).
[17] T. Chalopin, T. Satoor, A. Evrard, V. Makhalov, J. Dalibard, R. Lopes, and S. Nascimbene, Probing chiral edge dynamics and bulk topology of a synthetic Hall system, Nat. Phys. **16**, 1017 (2020).
[18] C.-H. Li, Y. Yan, S.-W. Feng, S. Choudhury, D. B. Blasing, Q. Zhou, and Y. P. Chen, Bose-Einstein condensate on a synthetic topological Hall cylinder, PRX Quantum **3**, 010316 (2022).
[19] S. Kolkowitz, S. L. Bromley, T. Bothwell, M. L. Wall, G. E. Marti, A. P. Koller, X. Zhang, A. M. Rey, and J. Ye, Spin–orbit-coupled fermions in an optical lattice clock, Nature (London) **542**, 66 (2017).
[20] L. F. Livi, G. Cappellini, M. Diem, L. Franchi, C. Clivati, M. Frittelli, F. Levi, D. Calonico, J. Catani, M. Inguscio, and L. Fallani, Synthetic Dimensions and Spin-Orbit Coupling with an Optical Clock Transition, Phys. Rev. Lett. **117**, 220401 (2016).
[21] S. L. Bromley, S. Kolkowitz, T. Bothwell, D. Kedar, A. Safavi-Naini, M. L. Wall, C. Salomon, A. M. Rey, and J. Ye, Dynamics of interacting fermions under spin–orbit coupling in an optical lattice clock, Nat. Phys. **14**, 399 (2018).
[22] X.-T. Lu, T. Wang, T. Li, C.-H. Zhou, M.-J. Yin, Y.-B. Wang, X.-F. Zhang, and H. Chang, Doubly Modulated Optical Lattice Clock: Interference and Topology, Phys. Rev. Lett. **127**, 033601 (2021).
[23] Z. Meng, L. Huang, P. Peng, D. Li, L. Chen, Y. Xu, C. Zhang, P. Wang, and J. Zhang, Experimental Observation of a Topological Band Gap Opening in Ultracold Fermi Gases with Two-Dimensional Spin-Orbit Coupling, Phys. Rev. Lett. **117**, 235304 (2016).
[24] C.-R. Yi, L. Zhang, L. Zhang, R.-H. Jiao, X.-C. Cheng, Z.-Y. Wang, X.-T. Xu, W. Sun, X.-J. Liu, S. Chen, and J.-W. Pan, Observing Topological Charges and Dynamical Bulk-Surface Correspondence with Ultracold Atoms, Phys. Rev. Lett. **123**, 190603 (2019).
[25] A. Valdés-Curiel, D. Trypogeorgos, Q.-Y. Liang, R. P. Anderson, and I. B. Spielman, Topological features without a lattice in Rashba spin-orbit coupled atoms, Nat. Commun. **12**, 593 (2021).
[26] Q.-Y. Liang, D. Trypogeorgos, A. Valdés-Curiel, J. Tao, M. Zhao, and I. B. Spielman, Coherence and decoherence in the Harper-Hofstadter model, Phys. Rev. Research **3**, 023058 (2021).
[27] R. Zhang, Y. Yan, and Q. Zhou, Localization on a Synthetic Hall Cylinder, Phys. Rev. Lett. **126**, 193001 (2021).
[28] A. Fabre, J.-B. Bouhiron, T. Satoor, R. Lopes, and S. Nascimbene, Laughlin's Topological Charge Pump in an Atomic Hall Cylinder, Phys. Rev. Lett. **128**, 173202 (2022).
[29] Z.-Y. Wang, X.-C. Cheng, B.-Z. Wang, J.-Y. Zhang, Y.-H. Lu, C.-R. Yi, S. Niu, Y. Deng, X.-J. Liu, S. Chen, and J.-W. Pan, Realization of an ideal Weyl semimetal band in a quantum gas with 3D spin-orbit coupling, Science **372**, 271 (2021).
[30] Z. Ren, D. Liu, E. Zhao, C. He, K. K. Pak, J. Li, and G.-B. Jo, Chiral control of quantum states in non-Hermitian spin–orbit-coupled fermions, Nat. Phys. **18**, 385 (2022).
[31] E. J. Meier, F. A. An, and B. Gadway, Atom-optics simulator of lattice transport phenomena, Phys. Rev. A **93**, 051602(R) (2016).
[32] F. A. An, B. Sundar, J. Hou, X.-W. Luo, E. J. Meier, C. Zhang, K. R. A. Hazzard, and B. Gadway, Nonlinear Dynamics in a Synthetic Momentum-State Lattice, Phys. Rev. Lett. **127**, 130401 (2021).
[33] E. J. Meier, F. A. An, and B. Gadway, Observation of the topological soliton state in the Su–Schrieffer–Heeger model, Nat. Commun. **7**, 13986 (2016).
[34] F. A. An, E. J. Meier, and B. Gadway, Direct observation of chiral currents and magnetic reflection in atomic flux lattices, Sci. Adv. **3**, e1602685 (2017).
[35] D. Xie, W. Gou, T. Xiao, B. Gadway, and B. Yan, Topological characterizations of an extended Su–Schrieffer–Heeger model, npj Quantum Inf. **5**, 55 (2019).
[36] D. Xie, T.-S. Deng, T. Xiao, W. Gou, T. Chen, W. Yi, and B. Yan, Topological Quantum Walks in Momentum Space with a Bose-Einstein Condensate, Phys. Rev. Lett. **124**, 050502 (2020).
[37] S. K. Kanungo, J. D. Whalen, Y. Lu, M. Yuan, S. Dasgupta, F. B. Dunning, K. R. A. Hazzard, and T. C. Killian, Realizing topological edge states with Rydberg-atom synthetic dimensions, Nat. Commun. **13**, 972 (2022).
[38] C. Oliver, A. Smith, T. Easton, G. Salerno, V. Guarrera, N. Goldman, G. Barontini, and H. M. Price, Bloch oscillations along a synthetic dimension of atomic trap states, arXiv:2112.10648.
[39] N. R. Cooper and R. Moessner, Designing Topological Bands in Reciprocal Space, Phys. Rev. Lett. **109**, 215302 (2012).
[40] H. L. Stormer, D. C. Tsui, and A. C. Gossard, The fractional quantum Hall effect, Rev. Mod. Phys. **71**, S298 (1999).
[41] N. R. Cooper and J. Dalibard, Reaching Fractional Quantum Hall States with Optical Flux Lattices, Phys. Rev. Lett. **110**, 185301 (2013).
[42] Y. Yan, S.-L. Zhang, S. Choudhury, and Q. Zhou, Emergent Periodic and Quasiperiodic Lattices on Surfaces of Synthetic Hall Tori and Synthetic Hall Cylinders, Phys. Rev. Lett. **123**, 260405 (2019).

[43] R. P. Anderson, D. Trypogeorgos, A. Valdés-Curiel, Q.-Y. Liang, J. Tao, M. Zhao, T. Andrijauskas, G. Juzeliūnas, and I. B. Spielman, Realization of a deeply subwavelength adiabatic optical lattice, Phys. Rev. Research **2**, 013149 (2020).

[44] M. A. Khamehchi, C. Qu, M. E. Mossman, C. Zhang, and P. Engels, Spin-momentum coupled Bose-Einstein condensates with lattice band pseudospins, Nat. Commun. **7**, 10867 (2016).

[45] R. Rosa-Medina, F. Ferri, F. Finger, N. Dogra, K. Kroeger, R. Lin, R. Chitra, T. Donner, and T. Esslinger, Observing Dynamical Currents in a Non-Hermitian Momentum Lattice, Phys. Rev. Lett. **128**, 143602 (2022).

[46] N. R. Cooper, Optical Flux Lattices for Ultracold Atomic Gases, Phys. Rev. Lett. **106**, 175301 (2011).

[47] J. H. Han, J. H. Kang, and Y. Shin, Band Gap Closing in a Synthetic Hall Tube of Neutral Fermions, Phys. Rev. Lett. **122**, 065303 (2019).

[48] S. Omanakuttan, A. Mitra, M. J. Martin, and I. H. Deutsch, Quantum optimal control of ten-level nuclear spin qudits in ^{87}Sr, Phys. Rev. A **104**, L060401 (2021).

[49] J. B. Naber, L. Torralbo-Campo, T. Hubert, and R. J. C. Spreeuw, Raman transitions between hyperfine clock states in a magnetic trap, Phys. Rev. A **94**, 013427 (2016).

[50] S. Zhang and G.-B. Jo, Recent advances in spin-orbit coupled quantum gases, J. Phys. Chem. Solids **128**, 75 (2019).

[51] See Supplemental Material at http://link.aps.org/supplemental/10.1103/PhysRevLett.128.245301 for more details, which includes Refs. [52–62].

[52] L. Petzold, Automatic selection of methods for solving stiff and nonstiff systems of ordinary differential equations, SIAM J. Sci. Stat. Comput. **4**, 136 (1983).

[53] M. Kasevich and S. Chu, Measurement of the gravitational acceleration of an atom with a light-pulse atom interferometer, Appl. Phys. B **54**, 321 (1992).

[54] T. Mukaiyama, H. Katori, T. Ido, Y. Li, and M. Kuwata-Gonokami, Recoil-Limited Laser Cooling of ^{87}Sr Atoms Near the Fermi Temperature, Phys. Rev. Lett. **90**, 113002 (2003).

[55] N. Q. Burdick, Y. Tang, and B. L. Lev, Long-Lived Spin-Orbit-Coupled Degenerate Dipolar Fermi Gas, Phys. Rev. X **6**, 031022 (2016).

[56] L. Hu, E. Wang, L. Salvi, J. N. Tinsley, G. M. Tino, and N. Poli, Sr atom interferometry with the optical clock transition as a gravimeter and a gravity gradiometer, Classical Quantum Gravity **37**, 014001 (2020).

[57] B.-Z. Wang, Y.-H. Lu, W. Sun, S. Chen, Y. Deng, and X.-J. Liu, Dirac-, Rashba-, and Weyl-type spin-orbit couplings: Toward experimental realization in ultracold atoms, Phys. Rev. A **97**, 011605(R) (2018).

[58] Z. Wu, L. Zhang, W. Sun, X.-T. Xu, B.-Z. Wang, S.-C. Ji, Y. Deng, S. Chen, X.-J. Liu, and J.-W. Pan, Realization of two-dimensional spin-orbit coupling for Bose-Einstein condensates, Science **354**, 83 (2016).

[59] W. Sun, B.-Z. Wang, X.-T. Xu, C.-R. Yi, L. Zhang, Z. Wu, Y. Deng, X.-J. Liu, S. Chen, and J.-W. Pan, Highly Controllable and Robust 2D Spin-Orbit Coupling for Quantum Gases, Phys. Rev. Lett. **121**, 150401 (2018).

[60] M. M. Boyd, High Precision spectroscopy of strontium in an optical lattice: Towards a new standard for frequency and time, Ph.D. thesis, University of Colorado, 2007.

[61] D. A. Steck, *Quantum and Atom Optics* (University of Colorado, Eugene, 2021).

[62] M.-C. Liang, Y.-D. Wei, L. Zhang, X.-J. Wang, H. Zhang, W.-W. Wang, W. Qi, X.-J. Liu, and X. Zhang, Realization of Qi-Wu-Zhang model in spin-orbit-coupled ultracold fermions, arXiv:2109.08885.

[63] S. Stellmer, Degenerate quantum gases of strontium, Ph.D. thesis, University of Innsbruck, 2013.

[64] S. Snigirev, A. J. Park, A. Heinz, I. Bloch, and S. Blatt, Fast and dense magneto-optical traps for strontium, Phys. Rev. A **99**, 063421 (2019).

[65] F. Scazza, Probing SU(N)-symmetric orbital interactions with ytterbium Fermi gases in optical lattices, Ph.D. thesis, Ludwig Maximilian University of Munich, 2015.

[66] J. D. Whalen, S. K. Kanungo, R. Ding, M. Wagner, R. Schmidt, H. R. Sadeghpour, S. Yoshida, J. Burgdörfer, F. B. Dunning, and T. C. Killian, Probing nonlocal spatial correlations in quantum gases with ultra-long-range Rydberg molecules, Phys. Rev. A **100**, 011402(R) (2019).

[67] S. Stellmer, R. Grimm, and F. Schreck, Detection and manipulation of nuclear spin states in fermionic strontium, Phys. Rev. A **84**, 043611 (2011).

[68] We do not expect this sweep rate to be adiabatic with respect to the current Rabi coupling strengths.

[69] D. S. Barker, Degenerate gases of strontium for studies of quantum magnetism, Ph.D. thesis, University of Maryland, College Park, 2016.

[70] B. Song, C. He, S. Zhang, E. Hajiyev, W. Huang, X.-J. Liu, and G.-B. Jo, Spin-orbit-coupled two-electron Fermi gases of ytterbium atoms, Phys. Rev. A **94**, 061604(R) (2016).

[71] P. Wang, Z.-Q. Yu, Z. Fu, J. Miao, L. Huang, S. Chai, H. Zhai, and J. Zhang, Spin-Orbit Coupled Degenerate Fermi Gases, Phys. Rev. Lett. **109**, 095301 (2012).

[72] D. L. Campbell, G. Juzeliūnas, and I. B. Spielman, Realistic Rashba and Dresselhaus spin-orbit coupling for neutral atoms, Phys. Rev. A **84**, 025602 (2011).

[73] D. L. Campbell and I. B. Spielman, Rashba realization: Raman with RF, New J. Phys. **18**, 033035 (2016).

[74] H. M. Price and N. R. Cooper, Mapping the Berry curvature from semiclassical dynamics in optical lattices, Phys. Rev. A **85**, 033620 (2012).

[75] P. Lauria, W. Kuo, N. Cooper, and J. Barreiro, Experimental realization of a fermionic spin-momentum lattice [Dataset and Code] 2022, 10.17863/CAM.84678.

[76] J. Aman, Two-photon photoassociative spectroscopy of strontium-86, Ph.D. thesis, Rice University, 2019.